



Characterization of a huge transatlantic smoke transport event by constructing an Aeolus smoke dataset in synergy with multi-platform data

5 Kangwen Sun^{1,2}, Guangyao Dai¹, Dimitri Traпон², Holger Baars², Albert Ansmann², Ulla Wandinger²,
Songhua Wu^{1,3,4}

¹College of Marine Technology, Faculty of Information Science and Engineering, Ocean University of China, Qingdao, China

²Leibniz Institute for Tropospheric Research (TROPOS), Leipzig, Germany

³Laoshan Laboratory, Qingdao, China

⁴Institute for Advanced Ocean Study, Ocean University of China, Qingdao, China

10 *Correspondence to:* Songhua Wu (wush@ouc.edu.cn)

Abstract. During the wildfire season on the West Coast of the US in September 2020, biomass burning smoke aerosol was continually generated, and several transatlantic smoke transports occurred. The ALADIN lidar onboard Aeolus satellite measured global wind and aerosol profiles from August 2018 to April 2023. As a high spectral resolution lidar (HSRL), ALADIN could directly retrieve the extinction coefficient. Targeting a large-scale tropospheric smoke transport event originating from the western US on 14 September and arriving over Europe on 21 September, a method for constructing an Aeolus smoke dataset was developed based on ALADIN observations, in synergy with multi-platform data. The backscatter coefficient in the smoke dataset was corrected using a linear depolarization ratio of 0.15, since ALADIN detected only co-polarized backscattered signals and the averaged smoke depolarization ratio remained relatively stable throughout the transport. Utilizing the selected cross-sections from the Aeolus smoke dataset, we acquired the vertical structure of the smoke layers and characterized their features. These layers show good agreement with the HYSPLIT simulations and are considered representative of different transport phases. Statistical analyses of the complete Aeolus smoke dataset from 14 to 21 September reveal the evolution of the smoke plume throughout its transatlantic transport. We illustrated the variations in aerosol optical depth, layer altitude and lidar ratio throughout the transport process. To our knowledge, this paper represents the first use of a spaceborne HSRL for observations and analyses of a large-scale tropospheric smoke transport. The comprehensive characterization presented offers valuable information for advancing global aerosol research.

1 Introduction

Smoke aerosols, primarily produced by biomass burning events such as wildfires, exert significant impacts on the Earth system by perturbing the radiation balance, influencing cloud formation, and degrading air quality (Sokolik et al., 2019; Ditas et al., 2018; Hirsch & Koren, 2021). In recent years, climate change has driven hotter and drier conditions and more frequent wildfires, leading to the formation of increasingly intense smoke layers in the atmosphere (Kirchmeier-Young et al., 2019; Cunningham



et al., 2024; Trickl et al., 2024). Smoke aerosols from wildfires can be lofted to altitudes of up to ~35 km, thereby inducing substantial perturbations to tropospheric cloud processes and stratospheric aerosol composition (Khaykin et al., 2020; Twohy et al., 2021; Peterson et al., 2021). Once injected, smoke plumes can undergo long-range transport via large-scale atmospheric circulation, affecting regions far from their sources. Accurately representing such long-range transport is therefore essential
35 for the parameterization of cloud–aerosol interactions in regional and global models, ultimately improving the fidelity of weather and climate predictions (Lohmann and Neubauer, 2018; Beer et al., 2022, 2024).

Lidar remote sensing is an effective approach for atmospheric measurements, providing vertically resolved parameters and information. Based on ground-based lidar observations, extensive research has been conducted to investigate the characteristics of smoke aerosols and their environmental impacts. Using lidar measurements at Leipzig, Haarig et al. (2018) characterized
40 the properties of aged tropospheric and stratospheric smoke originating from Canadian wildfire. The impacts of wildfire smoke aerosols on cirrus formation over the eastern Mediterranean and the Arctic were explored by Mamouri et al. (2023) and Ansmann et al. (2025), based on lidar observations. Wildfire smoke was found contributing to the processes driving record-breaking stratospheric ozone depletion over the Arctic and Antarctica in 2020 (Ohneiser et al., 2021). Therefore, with the observation records of single ground-based lidar station, 1) smoke plumes at specific phase of the whole development or
45 transport process can be characterized in detail, meanwhile 2) interactions between smoke layers and other atmospheric constituents, such as clouds or ozone, can be investigated. Furthermore, lidar networks, comprising multiple stations, have increasingly been employed in wildfire smoke research. Floutsi et al. (2023) derived universal lidar-based intensive optical properties of smoke aerosols - including the particle linear depolarization ratio, the extinction-to-backscatter ratio (lidar ratio), and the Ångström exponent - by analyzing long-term observations from the European Aerosol Research Lidar Network
50 (EARLINET) and several dedicated campaigns. Vaughan et al. (2018) and Baars et al. (2019) utilized the observations of the UK lidar network and the EARLINET individually, characterizing the smoke aerosols transported from North America. Although lidar sites can provide information on smoke over different regions, they primarily capture the decay phase of transport rather than the entire transport process. In summary, ground-based lidar stations and networks are valuable for investigating smoke processes over specific regions and for establishing comprehensive smoke databases, but they are limited
55 in their ability to track long-range smoke transport.

For tracking long-distance smoke transport, particularly across oceans, satellite-based lidars provide valuable global measurements, as most operate in polar orbits and circle the Earth more than ten times per day. The Cloud-Aerosol Lidar with Orthogonal Polarization (CALIOP) aboard the Cloud-Aerosol Lidar and Infrared Pathfinder Satellite Observation (CALIPSO) mission measured global vertical profiles of atmospheric aerosol and cloud optical properties from 2006 to 2023 (Winker et al., 2009; Omar et al., 2009). Using three measurement cross-sections, Vaughan et al. (2018) tracked a wildfire smoke plume
60 originating in western Canada in May 2016 then it crossed the Atlantic to the UK, finding that the plumes were primarily transported in the middle troposphere (3 to 11 km) with a slight ascending tendency, and that the smoke aerosol depolarization ratios at 532 nm remained below 0.1. Similarly, a wildfire smoke transport event from Canada to Europe in May - June 2019 was characterized by analyzing CALIOP profiles divided by west-to-east locations (Shang et al., 2024), revealing that 1)



65 transport occurred mainly in the middle troposphere (3 to 8 km), 2) aerosol optical depth (AOD) at 532 nm decreased from
0.25 to near zero, and 3) depolarization ratio at 532 nm increased from 0.03 to 0.06. Focusing on smoke self-lofting, Ohneiser
et al. (2023) examined CALIOP cross-sections of Canadian wildfire smoke in 2017 and Australian smoke in 2020, showing
plumes lofted from 12 to 13 km to around 20 km due to absorbing solar radiation, indicating the transports were in the upper
troposphere and lower stratosphere. Collectively, these studies demonstrate that CALIOP measurements enable detailed
70 tracking and characterization of long-range wildfire smoke transport. Nevertheless, as an elastic-backscatter lidar, CALIOP-
derived extinction coefficients and AOD rely on assumptions of the extinction-to-backscatter ratio (lidar ratio) (Kim et al.,
2018).

As the first wind spaceborne lidar and also the first operated spaceborne high spectral resolution lidar, the Atmospheric Laser
Doppler Instrument (ALADIN) onboard Aeolus satellite measured global wind and aerosol profiles simultaneously for more
75 than 4 years (August 2018 to April 2023) (Stoffelen et al., 2005; Reitebuch, 2012). The aerosol and cloud optical properties
product (Level 2A) of Aeolus includes directly derived extinction coefficient and co-polarized backscatter coefficient profiles
at 355 nm, transmits circularly polarized light but measures only the co-polarized component of the backscattered light
(Flament et al., 2021). Aeolus Level 2A product has been involved in the research of the characterization of dust aerosols and
the evaluation of the wind impact on marine aerosol (Song et al., 2024; Sun et al., 2024). It also provides opportunity to track
80 and describe large-scale long-range aerosol transport with the underlying possible dynamic reasons described by the wind
information. Based on Aeolus data, Dai et al. (2022) captured and analyzed a huge dust transport event from the Sahara dust
crossing the Atlantic to the Caribbean Sea occurred in June 2020. The dust plumes were found below 6 km during transport
and the wind vector product (Level 2C) from Aeolus was also used to evaluate the transport intensity. In this study, a huge
smoke transport stage in September 2020 will be focused on, of which the smoke aerosols were generated from the extreme
85 forest fires in California (Hu et al., 2022; Ceamanos et al., 2023; Eck et al., 2023). It has been reported that the smoke plumes
were transported to Europe crossing Atlantic and the whole transport stage may include two distinct transport processes with
the period of 5-7 days (Hu et al., 2022). Aeolus Level 2A product has demonstrated the capability to measure smoke profiles
(Baars et al., 2021). However, during long-range transport, smoke plumes may become mixed with other aerosols and clouds.
Moreover, Aeolus's ability to classify aerosols and clouds was limited due to the absence of depolarization measurements.
90 Based on Aeolus product, together with CALIOP, spaceborne passive instruments (Visible Infrared Imaging Radiometer Suite,
VIIRS; Moderate-resolution Imaging Spectroradiometer, MODIS), models (Modern-Era Retrospective analysis for Research
and Applications, Version 2, MERRA-2; Hybrid Single Particle Lagrangian Integrated Trajectory Model, HYSPLIT), this
study 1) determined the general region and period of the smoke transport, 2) derived the Aeolus smoke profiles and conducted
validation, 3) selected the Aeolus cross-sections to characterize the smoke layers in different transport phases, and 4)
95 investigated the features of the entire smoke event using all Aeolus smoke profiles in the transport region. The derived Aeolus
smoke profiles dataset mainly include backscatter coefficient, extinction coefficient and lidar ratio. The correction of
backscatter coefficient was conducted using a linear depolarization ratio of 0.15 since the average smoke depolarization ratio
remained relatively stable throughout the transport.



2 Data and model

100 2.1 ALADIN

During its operational lifetime from August 2018 to April 2023, the ALADIN instrument onboard the Aeolus satellite provided global atmospheric wind measurements along with aerosol and cloud observations simultaneously for more than 4 years, covering the atmospheric column from the surface to the lower stratosphere. As a high spectral resolution lidar operating at a wavelength of 354.8 nm, ALADIN had the capability to separate atmospheric particulate (aerosol and cloud) backscattered signal from molecular backscattered signal (Reitebuch et al., 2012). Thus, extinction coefficients can be retrieved directly without the need to assume a lidar ratio. However, ALADIN was not equipped with a cross-polar polarization detection channel, resulting in the absence of polarization information in its backscatter measurements (Flament et al., 2021). Further details on the instrument design and the measurement concept have been reported in Ansmann et al. (2007), Dabas et al. (2008), Flamant et al. (2008), Reitebuch (2012), Lux et al. (2020), and Flament et al. (2021).

105

110 Aeolus data products include several different levels: Level 0 (instrument housekeeping data), Level 1B (engineering-corrected HLOS winds), Level 2A (aerosol and cloud layer optical properties, including particulate extinction coefficient α , backscatter coefficient β , and lidar ratio, all at 355 nm), Level 2B (meteorologically representative HLOS winds) and Level 2C (Aeolus-assisted wind vectors) (Flamant et al., 2008; Tan et al., 2008; Rennie et al., 2020). “Baselines” of the products were defined to represent the products retrieved with different processor versions. Up to the time of this study, the products of Level 2A

115 Baseline 16 with the time period of Aeolus’ whole lifetime have been published (<https://aeolus-ds.eo.esa.int/oads/access/>; last access: 27 August 2025). The Level 2A Baseline 16 product includes aerosol and cloud retrievals derived from various algorithms. Among them, the SCA is a retrieval algorithm using a direct algebraic inversion scheme, and the SCAMid is a version using better vertical averaging strategy, of which the products were more recommended for usage than the initial one (Flament et al., 2021, Gkikas et al., 2023). The Mie Channel Algorithm MCA relies on Mie signal only and provides particle

120 extinction assuming a fixed lidar ratio. The Maximum Likelihood Estimation (MLE) and the MLEsub algorithms, based on physically constrained optimal estimation, found denoised aerosol retrievals when compared to SCA and SCAMid, especially for the particles extinction coefficient (Ehlers et al., 2022; Trapon et al., 2025). The data with the MLEsub has higher horizontal resolution (18 km) than the one with the MLE (90 km). The AEL-PRO algorithm was developed targeting the Earth Cloud Aerosol and Radiation Explorer (EarthCARE) HSRL ATmospheric LIDar (ATLID), based on the feature mask identification

125 as the previous step (Wang et al., 2024). In this study, α and β in the Level 2A product with the MLE algorithm and aligned with 90 km horizontal from Baseline 16 were adopted. The vertical resolution varies from 0.25 km close to the surface to 2 km for top height, with most range bin thickness aligned with 0.5 km, 0.75 km and 1 km in upper troposphere. Relative humidity (RH) and molecular backscatter coefficient (β_m) from European Centre for Medium-Range Weather Forecasts Reanalysis 5 (ERA5) with the same grid of Aeolus measurement data provided in the Level 2A products are also used as the

130 auxiliary data.



2.2 CALIOP

CALIOP on board CALIPSO measured global aerosol and cloud vertical profiles for around 17 years from June 2006 to June 2023. CALIOP Level 2 Aerosol Profile products provide directly retrieved backscatter coefficient at 532 nm and particulate depolarization ratio at 532 nm. In this study, the Aerosol Profile products of data version 4.21 were used to evaluate the stability of the depolarization ratio during the smoke transport. The vertical resolution of the Aerosol Profile products is variable in the altitude region of 0.5 km to 30.1 km: 60 m for -0.5 km to 20.2 km, 180 m for 20.2 km to 30.1 km (Hunt et al., 2009). The horizontal resolution is 5 km. CALIOP Level 2 Vertical Feature Mask (VFM) products provide aerosol and cloud classification along the vertical profiles, consisting of the identification of aerosols and clouds, and further the subtypes of aerosols and clouds. The layer-integrated volume depolarization ratio at 532 nm, the layer-integrated total attenuated color ratio, the layer-averaged attenuated backscatter at 532 nm, the latitude and the altitude were taken account as the inputs of the cloud-aerosol discrimination (CAD) algorithm to distinguish aerosols from clouds (Liu et al., 2019). Aerosol bins were marked as “marine”, “dusty marine”, “dust”, “polluted dust”, “continental”, “polluted continental/smoke”, “elevated smoke”, and “others” according to the comprehensive analysis of the particulate depolarization ratio at 532 nm, the integrated attenuated backscatter coefficient at 532 nm, the layer top altitude, the layer base altitude, and the surface type (Kim et al., 2018). In this study, the VFM products from data version 4.21 were used. The spatial resolutions of VFM products are variable: 30 m vertically and 333 m horizontally for the altitude range of -0.5 km to 8.2 km, 60 m vertically and 1000 m horizontally for 8.2 km to 20.2 km, 180 m vertically and 1667 m horizontally for 20.2 km to 30.1 km (Hunt et al., 2009).

2.3 MODIS

MODIS instrument is a Moderate Resolution Imaging Spectroradiometer, designed for the measurement of atmosphere, ocean, and land, monitoring global data with 36 high spectral resolution bands between 0.415 and 14.235 μm with spatial resolutions of 250 m (2 bands), 500 m (5 bands), and 1000 m (29 bands) (Savtchenko et al., 2004). Two MODIS instruments on board Terra satellite (10:30 equator crossing time, descending) and Aqua satellite (13:30 equator crossing time, ascending) provide near-global daily observations. In this study, we used the merged “Deep Blue/Dark Target” AOD at 550 nm from both Terra and Aqua to get the best coverage, for the purpose of smoke plume localization and Aeolus products’ validation (Levy et al., 2013). The temporal resolution is daily and the spatial resolution is 1° .

2.4 VIIRS

Visible Infrared Imaging Radiometer Suite (VIIRS) onboard Suomi National Polar-Orbiting Partnership (S-NPP) satellite is a cross-track scanning radiometer with 22 spectral bands covering the visible/infrared spectrum (0.412–12.05 μm) (Liu et al., 2014). The satellite flies in a sun-synchronous polar orbit with the ascending equator crossing time of 13:30. The photo-like true-color images with the temporal resolution of daily and the spatial resolution of 250 m visualized by the Worldview (<https://worldview.earthdata.nasa.gov>, last access: 29 August 2025) were applied to localize the smoke plume.

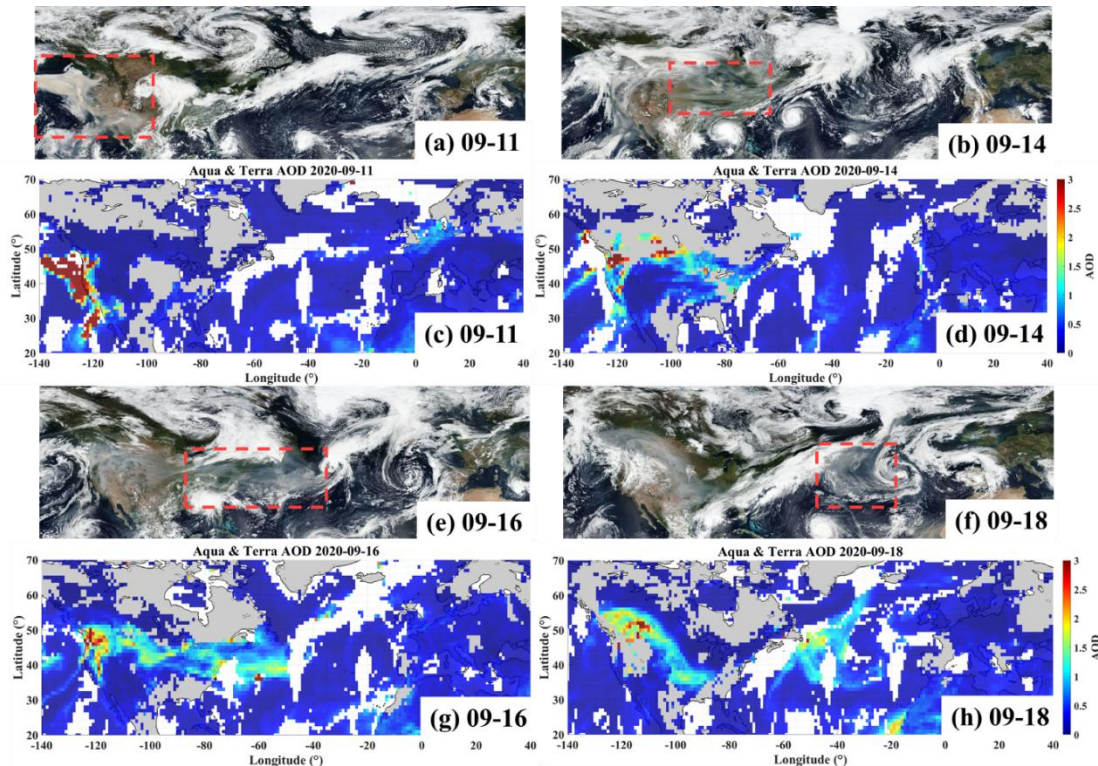
2.5 MERRA-2

The Modern-Era Retrospective Analysis for Research and Applications, version 2 (MERRA-2), is the atmospheric reanalysis of the modern satellite era produced by NASA's Global Modeling and Assimilation Office (GMAO), assimilated with more than 30 types of observation including both satellite and ground-based remote sensing (Gelaro et al. 2017). The hourly column mass concentration (CMC) of organic carbon, black carbon and dust with the spatial resolution of $0.5^\circ \times 0.625^\circ$ from MERRA-2 were utilized to extract smoke data of Aeolus observations.

2.6 HYSPLIT

The Hybrid Single-Particle Lagrangian Integrated Trajectory model (HYSPLIT) is a modeling system developed by the National Oceanic and Atmospheric Administration (NOAA) Air Resources Laboratory (ARL), which is capable to simulate the transport trajectories, dispersion and diffusion of air masses (Stein et al., 2015). In this study, both backward and forward trajectory simulations with model vertical velocity are applied to verify the pathway of smoke plume transport.

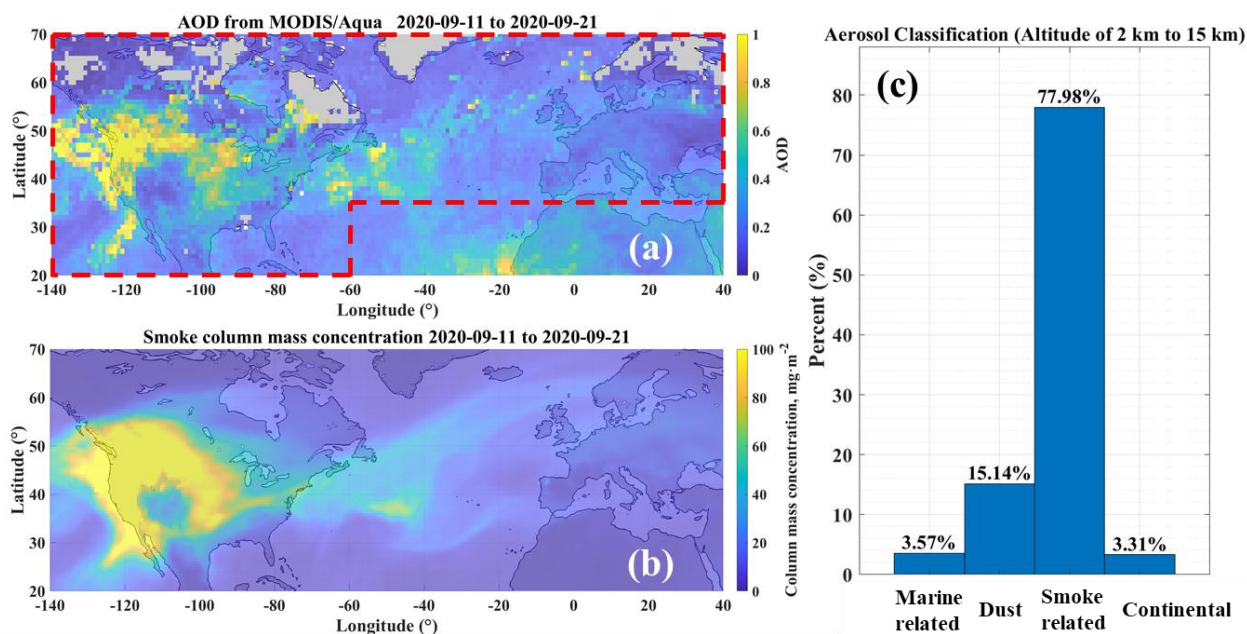
3 Localization of the smoke plume transport



175 **Figure 1.** Observations of spaceborne passive instruments in the spatial range of 140°W to 40°E and 20°N to 70°N . True-color images from VIIRS on (a) 11, (b) 14, (e) 16, (f) 18 September 2020, acquired on the Worldview (<https://worldview.earthdata.nasa.gov>, last access: 29 August 2025). Average AOD from both Aqua and Terra on (c) 11, (d) 14, (g) 16, (h) 18 September 2020.



In 2020, more than 8000 wildfires in the west coast of the US generated large amounts of smoke aerosol into the atmosphere continuously (<https://www.fire.ca.gov/incidents/2020/>, last access: 30 August 2025). A pronounced smoke transport process from the western US across the Atlantic to Europe in September is presented and illustrated in Fig. 1. The daily true-color images from VIIRS and the daily mean AOD derived from Aqua and Terra are shown in this figure. The red dashed region in panel (a) highlights a clearly visible, dense smoke plume over the west coast. Consistent with this observation, panel (c) indicates that many of the associated smoke layers reached AOD values greater than 3. In panels (b), (e), and (f), the visible smoke plumes within the red dashed boxes indicate smoke plumes generated off the west coast of the US and moving above the Atlantic from September 14 to 18. The maximum AOD values could exceed 1.5 during transport, as shown in panels (d), (g), and (h). Hu et al. (2022) observed smoke layers at the lidar station ATOLL (ATmospheric Observatory of LiLle) in northern France, from 17 to 22 September, which were investigated transported from Oregon (located on the west coast of the US) starting on 13 September. This corresponds well with the smoke plume transport indicated in Fig.1, suggesting that the smoke plume was transported to Europe afterwards. In conclusion, the snapshots taken by spaceborne passive instruments captured the daily locations of smoke plumes during their transport from the west coast of the US across the Atlantic to Europe. However, passive instruments cannot provide vertical plume information, and AOD retrieval cannot be accomplished in the presence of clouds.



195 **Figure 2. (a) Average AOD by MODIS onboard Aqua; (b) Average smoke column mass concentration (CMC) by MERRA-2; (c) Statistical result of aerosol classification from CALIOP VFM products, taking the data in the region indicated by the red dashed box of panel (a). The temporal range is 11 to 21 September 2020.**

In order to further investigate the pathway of the entire smoke transport process, the averaged AOD and the smoke CMC with the same spatial coverage and the temporal range from 11 to 21 September 2020 are presented individually in panels (a) and



(b) of Fig. 2. The smoke CMC was calculated as the sum of the organic carbon and black carbon from the MERRA-2 reanalysis dataset. In general, these two figures align well for regions with high values, except for the Sahara Desert and the surrounding ocean, which have high load of atmospheric dust. From there figures, the transport pathway is visible. The smoke plume moved eastward from the west coast of the US, crossing the continental US and reaching the central Atlantic. Then, it separated into two branches. The larger branch moved northeastward over a longer distance, while the smaller one moved southeastward. The southern smoke plume was transported toward the Sahara Desert, where it may have mixed with dust aerosols. Overall, the gradual decrease in AOD and smoke CMC from west to east suggests that the concentration of the smoke aerosol diminished due to diffusion during its transport. However, it can be speculated that the accumulation of smoke plumes occurred over the Atlantic between longitude 70°W and 40°W after being transported away from land, as the AOD and the smoke CMC show higher values than the surrounding region. As previously mentioned, the Aeolus's ALADIN lidar cannot classify aerosol subtypes due to the lack of δ detection (Flament et al., 2021). Whether ALADIN can characterize the smoke plumes during transport depends on interference from other types of aerosols along the transport pathway. Therefore, an examination of the types of aerosols in the smoke pathway region was conducted. Data from the CALIOP VFM product was used. The aerosol subtype data within the altitude of 2 to 15 km and the period of 11 to 21 September, located in the red dashed box of Fig.2 (a), was counted for the statistical analysis. The result shown in Fig. 2 (c) indicates that the smoke-related aerosols (flagged as “elevated smoke”, “polluted continental/smoke”, “polluted dust” in the VFM product) dominate the region, accounting for around 78% of the total. Dust aerosol accounts for around 15%, while the sum of the others (marine-related and continental) accounts for less than 7%.

To conclude, in this section, we captured daily “snapshots” of the smoke plume during its transport from the west coast of the US across the Atlantic to the Europe. Furthermore, the specific period and pathway of the smoke transport were verified and the region was found dominated by the smoke-related aerosols.

220



4 Development and validation of the Aeolus-based smoke dataset

4.1 Collocation of multi-platform data

The AOD data from MODIS and the smoke CMC data from MERRA-2 are used for deriving and validating the Aeolus-based smoke dataset. Daily AOD averages are based on data from MODIS onboard Terra and Aqua. Due to the different spatial resolutions, these data were collocated to the Aeolus data grid, which follows the Aeolus orbit. The AOD data from MODIS used in this study is with a spatial resolution of 1° and a temporal resolution of one day. The smoke CMC data from MERRA-2 has a spatial resolution of $0.5^\circ \times 0.625^\circ$ and a temporal resolution of one hour. For the collocation, the temporal closest and spatial nearest data bins of AOD and smoke CMC to the Aeolus data grid, which has a horizontal resolution of 90 km along its orbits were selected. However, the time difference between Aeolus and MODIS can be several hours, while the difference between Aeolus and MERRA-2 can be tens of minutes, due to their distinct temporal resolutions.

4.2 Derivation of the smoke dataset from Aeolus observations

The extinction and backscatter coefficients measured by Aeolus contain information of both clouds and aerosols. In order to characterize the features and the evolution of the smoke plumes during transport, a smoke dataset including extinction coefficient, backscatter coefficient and lidar ratio from Aeolus observations should be acquired. Therefore, several steps were adopted to derive smoke data from the Aeolus L2A products:

- (1) Bins selection. The flag “bin-1-clear” inside the Aeolus L2A product was used for the preliminary quality control. Thresholds were set for the outlier elimination of backscatter and extinction coefficients. Backscatter coefficients larger than $30 \text{ Mm}^{-1}\text{sr}^{-1}$ and extinction coefficients larger than 600 Mm^{-1} were eliminated.
- (2) Cloud screening. We applied a similar method to that used in the marine aerosol research of Sun et al. (2024). Data bins with a backscatter ratio (R_b , calculated by total backscatter coefficient dividing molecular backscatter coefficient) higher than 2.5 are identified as cloud contamination. The threshold of RH was set more strictly than in Sun et al. (2024), such that clouds are considered to exist with a high possibility when RH is above 80% (Forbes et al., 2009). Consequently, Aeolus L2A data bins with R_b and RH no more than 2.5 and 80% are considered as aerosol data bins.
- (3) Smoke profiles selection. The Aeolus aerosol dataset from Aeolus L2A has been acquired by step 1 and 2. As introduced in Section 3, about 15% of the aerosols in the smoke transport region were dust. CMC data from MERRA-2 was utilized to select the L2A profiles with smoke aerosols. A Level 2A profile can be considered a “smoke profile” if it meets the following two criteria: a smoke CMC greater than 15 mg/m^2 and a smoke CMC proportion (calculated by the smoke CMC dividing the sum of the smoke CMC and the dust CMC) exceeding 60%.
- (4) Backscatter correction. Due to Aeolus missed the cross-polar component of the particle backscattered signals, the lidar ratio calculated directly by the original extinction and backscatter was overestimated. Thus, the correction is supposed to be performed in order to obtain the total backscatter coefficient. Additionally, as ALADIN was a circular polarization lidar system,



the smoke circular depolarization ratio ($\delta_{\text{smo, cir}}$) converted from $\delta_{\text{smo, lin}}$ should be used for the correction. The backscatter correction was accomplished applying the formulas below (Roy and Roy, 2008; Paschou et al., 2022):

$$\delta_{\text{smo, cir}} = \frac{2\delta_{\text{smo, lin}}}{1 - \delta_{\text{smo, lin}}} \quad (1)$$

$$255 \quad \beta_{\text{smo}} = (1 + \delta_{\text{smo, cir}})\beta_{\text{Aeolus}} \quad (2)$$

In terms of this smoke transport event, it has been investigated that the $\delta_{\text{smo, lin}}$ at 532 nm over the continental US is about 0.1 and the $\delta_{\text{smo, lin}}$ at 355 nm over the Europe is around 0.15 (Hu et al., 2022). The stability of $\delta_{\text{smo, lin}}$ during long transport, as well as the impact of their variation on total backscatter coefficient and lidar ratio should be discussed. Using the L2 APro product and L2 VFM product of CALIOP from 11 to 21 September, we examined the variation of $\delta_{\text{smo, lin}}$ in the smoke transport pathway. The particulate linear depolarization ratio data bins in the L2 APro product identified as the smoke-related aerosols (flagged as “elevated smoke”, “polluted continental/smoke”, “polluted dust” in the VFM product) were utilized for analysis. Since the transport was generally eastward, the red box region in panel (a) of Fig. 2 was divided into 9 sub-regions, each 20° wide zonally from 140°W to 40°E. The average $\delta_{\text{smo, lin}}$ values were calculated for these sub-regions. The highest value, 0.119, appeared in the subregion between 100°W and 80°W, while the lowest value, 0.110, appeared in the subregion between 20°W and 20°E. Basically, the average $\delta_{\text{smo, lin}}$ at 532 nm exhibits a slight decline trend from west to east during smoke transport. This variation is presented in Table A1 in the appendix. Therefore, we set the assumed linear depolarization ratio ($\delta_{\text{assu, lin}}$) at 355 nm to 0.15 for the entire transport process, slightly higher than the CALIOP measurements at 532 nm, to be in line with the observation of Hu et al. (2022) at 355 nm, but don’t anticipate significant variability as indicated by the CALIOP observations at 532 nm. Assuming a smoke bin with an extinction coefficient (α_{smo}) of 202.5 Mm⁻¹ and a Aeolus measured backscatter coefficient (β_{Aeolus}) of 3 Mm⁻¹sr⁻¹, with a $\delta_{\text{assu, lin}}$ of 0.15 (a assumed circular depolarization ratio ($\delta_{\text{assu, cir}}$) of 0.35), the measured total smoke backscatter coefficient (β_{meas}) can be calculated as 4.05 Mm⁻¹sr⁻¹, then the measured lidar ratio (L_{meas}) is 50 sr (a typical smoke lidar ratio at 355 nm). However, if there is a $\delta_{\text{assu, lin}}$ bias of 0.01 with the real linear depolarization ratio ($\delta_{\text{real, lin}}$) of 0.14 (the real circular depolarization ratio ($\delta_{\text{real, cir}}$) of 0.33), the real total smoke backscatter (β_{real}) can be calculated as 4 Mm⁻¹sr⁻¹ and the real lidar ratio (L_{real}) is 50.6 sr. In contrast, if the $\delta_{\text{real, lin}}$ is 0.16 ($\delta_{\text{real, cir}}$ is 0.38), β_{real} is 4.14 Mm⁻¹sr⁻¹ while L_{real} is 48.9 sr. Therefore, it can be summarized that, under these circumstances, if $\delta_{\text{real, lin}}$ varies from 0.14 to 0.16, then β_{real} will be within the range of 4 Mm⁻¹sr⁻¹ to 4.14 Mm⁻¹sr⁻¹ and L_{real} will be within the range of 48.9 sr to 50.6 sr. Namely, the L_{real} is around 50±1 sr when the $\delta_{\text{real, lin}}$ is 0.15±0.01. Assuming that the L_{meas} maintains a value of 50 sr and that the $\delta_{\text{real, lin}}$ declines by around 0.01 from 0.15 to 0.14 (assuming the same variation at 355 nm as at 532 nm throughout the entire transport), the constant $\delta_{\text{assu, lin}}$ at 355 nm of 0.15 could lead to an underestimation of the L_{meas} by the maximum error of around 1 sr. As shown in Table A1, the standard deviation of $\delta_{\text{smoke, lin}}$ at 532 nm can vary for an individual sub-region, with an approximate value of 0.085. Nevertheless, the corrected Aeolus β_{meas} and L_{meas} values are only used for the statistical analyses of a single measurement cross-section or a specific sub-region. Therefore, the effect of the assumed constant $\delta_{\text{assu, lin}}$ on β_{meas} and L_{meas} is considered negligible after averaging within each cross-section or sub-region.



(5) Lidar ratio calculation. Smoke lidar ratios were calculated for each data bin of smoke profiles by dividing extinction
285 coefficients by the corrected backscatter coefficients.

One cross-section example that was processed using the five steps above is shown in Fig. 3. This figure shows aerosol
extinction coefficients of Aeolus crossing the smoke plume on 15 September 2020. The black bins indicate the invalid values
while the gray ones indicate the cloud contaminated bins. They were all removed for subsequent characterization. Within the
red dashed lines, the “smoke profiles” captured a thick smoke layer alongside a cloud layer. The maximum altitude was around
290 12 km, and the latitude range was 33°N to 48°N (with a meridional width of more than 1500 km).

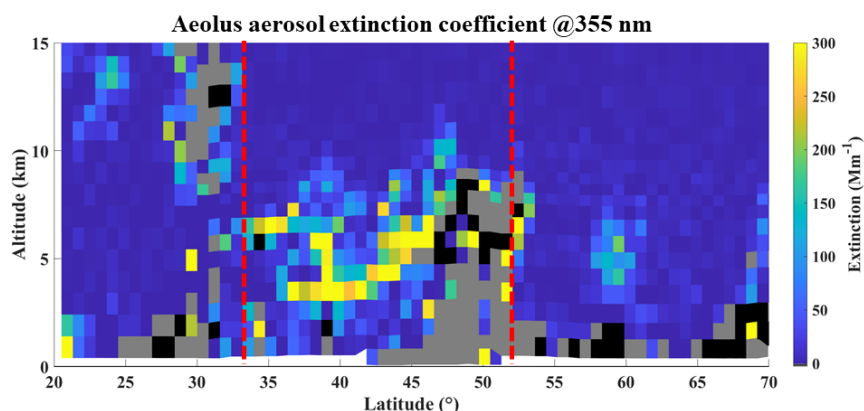


**Figure 3. One cross-section example of Aeolus aerosol extinction coefficient crossing the smoke plume, on 15 September 2020. The
corresponding orbit is presented in Fig. 5 (b). The data has been processed to derive smoke data from Aeolus by the steps introduced
in the section “Derivation of the smoke dataset from Aeolus observations”. The black bins indicate the invalid values, while the grey
ones indicate the cloud contaminated bins. The profiles inside two red dashed lines are the “smoke profiles”.**
295

4.3 Validation of the Aeolus smoke dataset

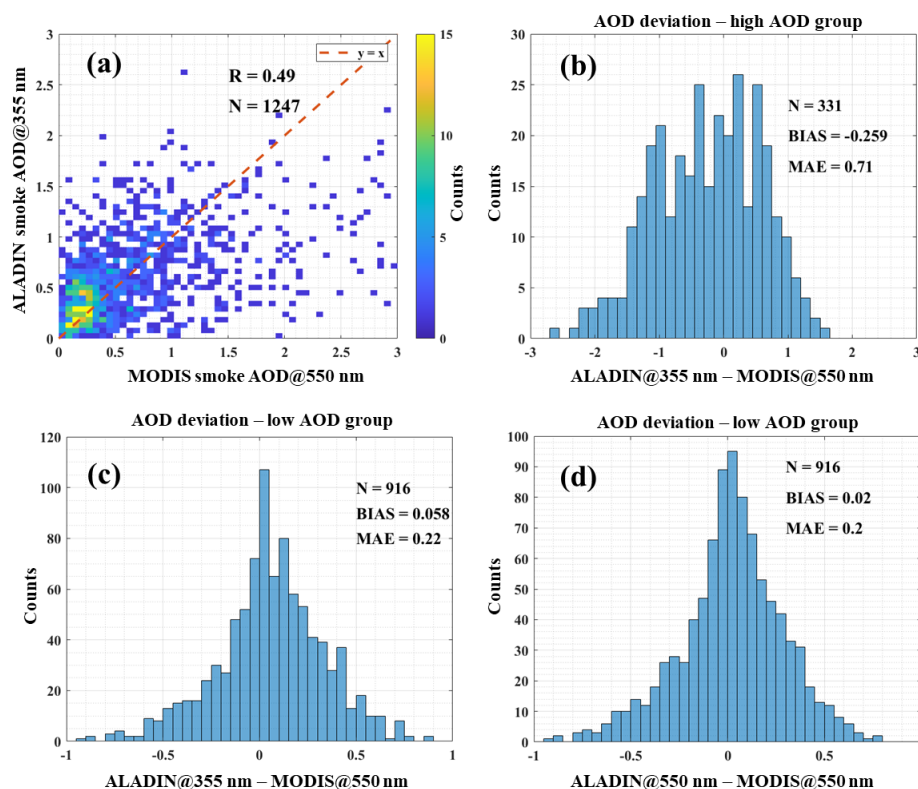
For the purpose of verify the reliability of the derived Aeolus smoke dataset, collocated AOD from MODIS was used for
validation. The validation dataset covers the period from 11 to 21 September 2020, and the spatial range is from 140°W to
40°E and 20°N to 70°N. Basically, the scatter between the MODIS AOD at 550 nm and the ALADIN AOD at 355 nm,
300 presented in Fig. 4 (a), indicates a reasonable degree of agreement, given their distinct measurement techniques, different
spatial grids and overpass times. However, when focusing on the AOD range of 0 to 0.5, it can be determined that the ALADIN
AODs are larger than the MODIS AODs, as more yellow bins indicating higher counts appear above the red dashed line
presenting the “y=x”. In addition, it is evident that the ALADIN AODs are generally less than 2 when the MODIS AODs range
from 2 to 3, illustrating that the MODIS AODs are higher than ALADIN when the AODs are relatively high. To investigate
305 more specifically, based on the above features, we separated the AODs into two groups based on AOD deviation (ALADIN
minus MODIS). The high AOD group consists of ALADIN AOD or MODIS AOD values larger than 1, while the low AOD
group consists of AOD values smaller than 1. The AOD deviation between the ALADIN (355 nm) and MODIS (550 nm)
measurements for the high and low AOD groups are presented in the histograms of panel (b) and panel (c) in Fig. 4. For the
high AOD group, the count number (N) of the matched pairs is 331, with a mean bias (BIAS) of -0.259 and a mean absolute



310 error of 0.71. It has been reported that, during severe smoke events, MODIS AOD (with either the Deep Blue or Dark Target
 algorithm) could overestimate the AOD when it is high (Gumber et al., 2023). With respect to the low AOD group, N is 916
 while BIAS is 0.058 and MAE is 0.22. The slight positive BIAS illustrates that the ALADIN AOD at 355 nm is larger than
 the MODIS AOD at 550 nm. This result is consistent with the Ångström power law (Ångström, 1964). In consideration of
 only smoke AOD is compared, the wavelength conversion was conducted. The Ångström exponent of 0.2 was applied to the
 315 conversion from 340 nm to 500 nm ($\text{ÅE}_{340-500}$), as reported by Hu et al. (2022) for the same smoke event. The low $\text{ÅE}_{340-500}$
 suggests that the smoke plumes could be dominated by the coarse mode aerosols. We also consider it acceptable to use ÅE_{340-}
 $_{500}$ for a similar wavelength range (355 nm to 550 nm), assuming the Ångström exponent is constant within the range of 340
 nm to 550 nm. The conversion was accomplished using the following formula:

$$\text{AOD}_{550 \text{ nm}} = \text{AOD}_{355 \text{ nm}} \exp(\text{ÅE}_{340-500} \ln \frac{355}{550}) \quad (2)$$

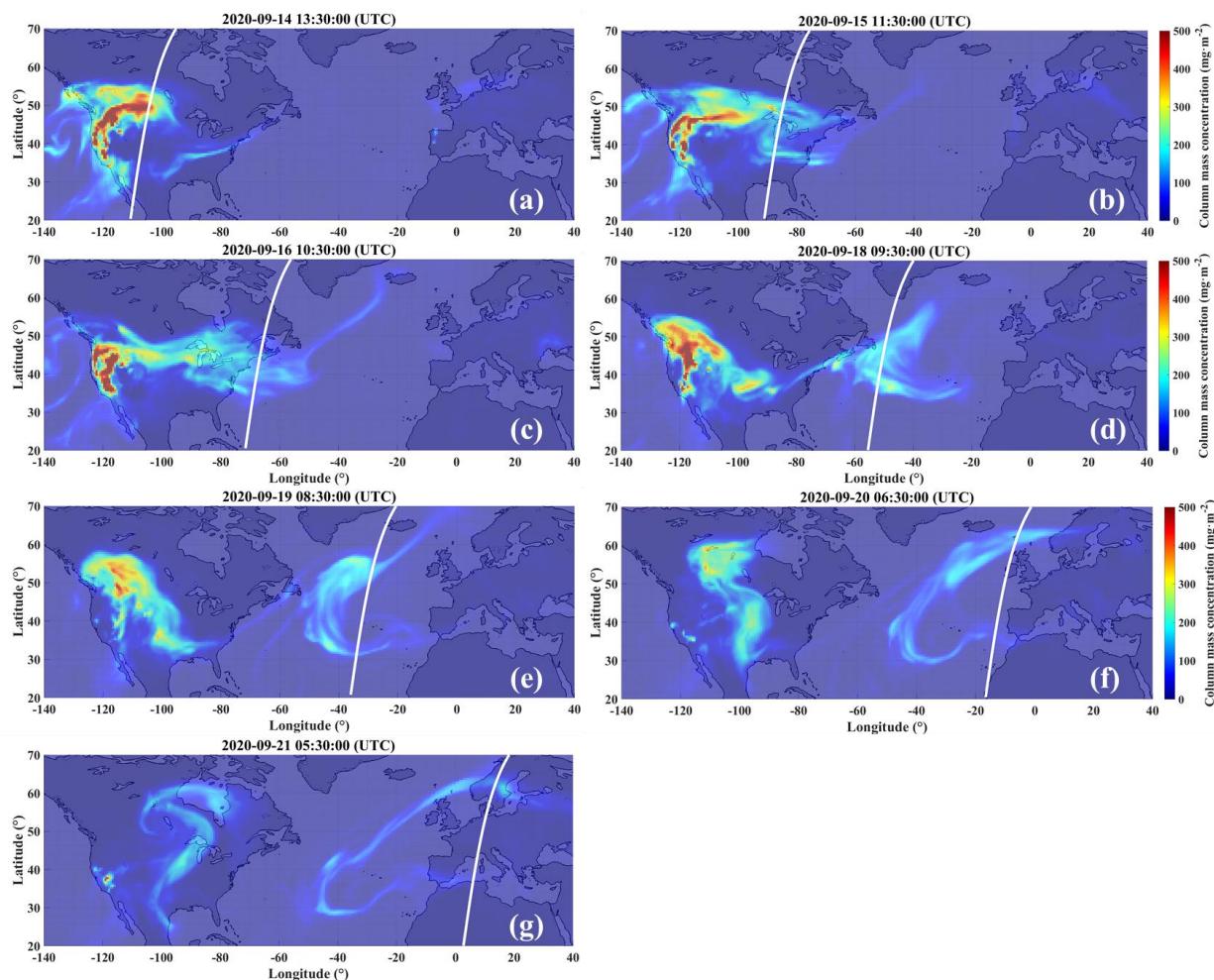
320 The AOD deviation between the converted ALADIN and MODIS AOD both at 550 nm is shown as the histogram in Fig. 4
 (d). The BIAS presents evident reduction to 0.02, while the MAE slightly decreased to 0.2. These results indicate better
 agreement and indicates that the AOD and extinction in the Aeolus smoke dataset are reliable.



325 **Figure 4. Comparison results between ALADIN and MODIS AOD. (a) Scatter of MODIS AOD at 550 nm and ALADIN AOD at 355 nm. AOD deviation histograms of ALADIN AOD at 355 nm minus MODIS AOD at 550 nm for (b) high AOD group and (c) low AOD group. (d) AOD deviation histograms of converted ALADIN AOD at 550 nm minus MODIS AOD at 550 nm for low AOD group.**

5 Characterization of the smoke transport

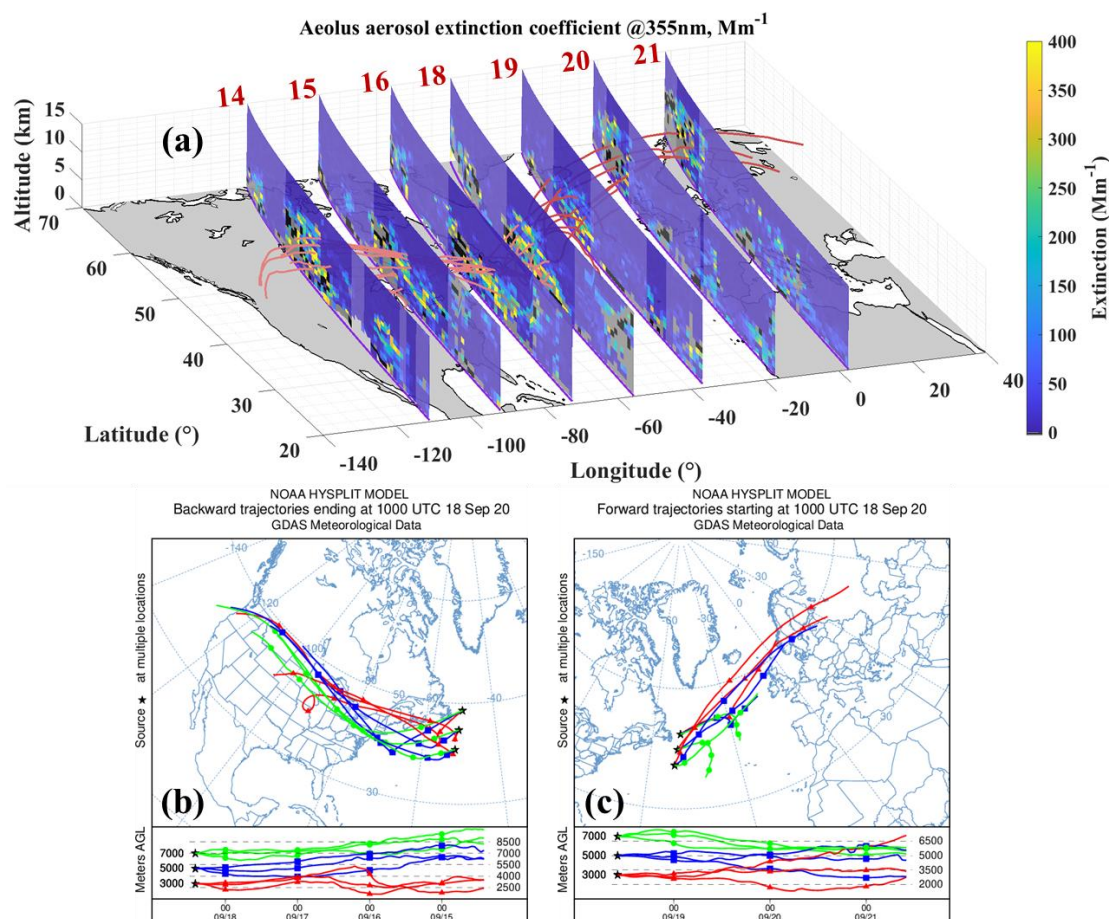
5.1 Cross-sections representing different transport phases



330

Figure 5. Smoke column mass concentration map in the spatial range of 140°W to 40°E, 20°N to 70°N, on (a) 14, (b) 15, (c) 16, (d) 18, (e) 19, (f) 20, (g) 21 September 2020, respectively. The white curves indicate the selected Aeolus orbits on the same days.

335 Seven Aeolus observations with descending orbits from west to east, from 14 to 21 September were selected, intended for the representing different phases of the smoke transport process. The locations of these cross-sections are shown as the white curves in Fig. 5, with the background smoke CMC maps temporally closest to every Aeolus orbit. From the smoke CMC maps, it can be clearly seen that a smoke plume generated from the west coast of the US, crossing the continental US and reached the Atlantic. There, it likely separated into two plumes. One of them, the larger one, arrived in Europe, while the other came to the Mediterranean. The seven Aeolus orbits, all of which cross the smoke plumes indicated by the smoke CMC maps, have the potential to capture cross-sections of the smoke plumes in different transport phases.



340

345

Figure 6. (a) The selected cross-sections of Aeolus aerosol extinction coefficient at 355 nm on 14, 15, 16, 18, 19, 20, 21 September 2020, with the HYSPLIT trajectories starting from 18 September. In the cross-sections, the black and grey bins indicate invalid data and cloud contaminated data separately, while the pink curves present the backward trajectories and the red curves are the forward trajectories. The dark parts of the curtains indicate smoke profiles identified by the step (3) in Section 4.2. Details of the (b) backward and (c) forward trajectories originating from the middle of the transport pathway (acquired by https://www.ready.noaa.gov/HYSPLIT_traj.php, last access: 7 September 2025).

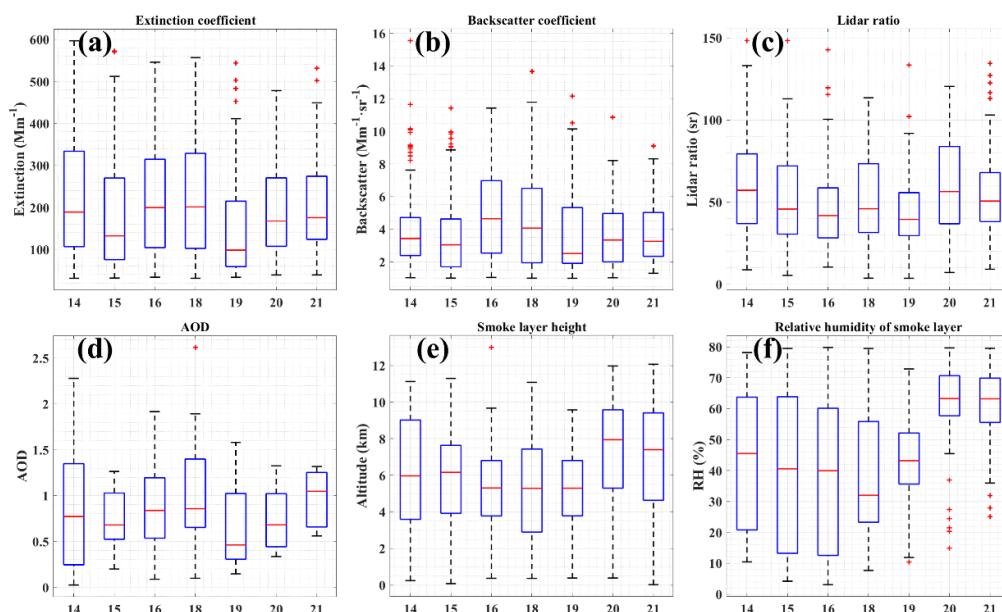
Figure 6(a) shows the seven selected cross-sections of the Aeolus aerosol extinction coefficient at 355 nm from September 14 to 21. The black bins indicate invalid data, and the white bins indicate cloud-contaminated data. The dark regions are considered to consist of "smoke profiles," but the bright regions did not meet the criteria introduced in Section 4.2 and were therefore not considered for further analysis. The backward and forward trajectories are also plotted in Fig. 6 (a), indicated by pink and red curves, respectively. The details of the trajectories are shown in Fig 6 (b) and (c). The starting time is 10:00 UTC on 18 September 2020 and the starting locations were determined by the smoke layers in the Aeolus cross-section on that day. The locations are 49.49°W, 48.55°N; 50.52°W, 44.62°N; and 51.44°W, 40.69°N. They are all in the smoke layers at altitudes of 3000 m, 5000 m, and 7000 m. The duration of the backward trajectories is 96 hours ending at 10:00 UTC on 14 September, while the duration of the forward trajectories is 72 hours ending at 10:00 UTC on 21 September. The cross-sections capturing

355



the smoke layers and the trajectories match well with each other, demonstrating the three-dimensional pathway of smoke transport. It can also be inferred that the smoke layers in the seven cross-sections are capable to represent the different transport phases. Regarding the smoke layers, it can be observed that, during the initial transport phases over the continental US on 14 and 15 September, the smoke plumes were accompanied by clouds on their northern sides. The main part of the smoke plume was transported northeast along the HYSPLIT trajectories after 18 September. However, in the cross-sections on 19 and 20 September, a few smoke layers were also identified and observed in the south region with latitudes between 30°N and 40°N, corresponding to the “plume separation” phenomenon found in the analyses of Fig.2 and Fig. 5. Only few smoke profiles were determined in this southern pathway, which might result from the smoke plume was weak and mixed with dust aerosol. In Fig. 6 (c), the two green curves turning to south could also illustrate the same phenomenon. On 20 and 21 September, the smoke plumes appeared to rise above the cloud layers according to Aeolus observations. However, the forward trajectory simulations underestimated the height of the smoke layer compared to the Aeolus observations.

To better characterize the smoke layers of the different transport phases, Fig. 7 presents boxplots of the extinction coefficient, backscatter coefficient, lidar ratio, aerosol optical depth (AOD), height, and relative humidity of the smoke layers in the cross-sections shown in Fig. 6(a). Only the northern smoke layers (if multiple smoke regions exist, e.g., in the cross-section of 14, 19 and 20 September) regarded in the main smoke plume pathway were selected for the calculation. More statistical results including the mean values and the corresponding standard deviations (std) of these parameters are summarized in Table 1. It should be emphasized that, only Aeolus smoke data bins with an extinction greater than 30 Mm^{-1} and a backscatter greater than 1 $\text{Mm}^{-1}\text{sr}^{-1}$ were considered representative of smoke layers and used in the statistical calculation.



375 **Figure 7.** The boxplots of (a) extinction coefficient, (b) backscatter coefficient, (c) lidar ratio, (d) AOD, (e) height and (f) relative humidity of the smoke layers in the cross-sections of Fig. 6 (a). Only the north smoke layers (if multiple smoke layers exist, e.g., in the cross-section of 14, 19 and 20) regarded in the main smoke plume pathway were selected for the calculation.



Table 1. Mean values and standard deviations of extinction coefficient, backscatter coefficient, lidar ratio, AOD, height and relative humidity, of the smoke layers in the cross-sections shown in Fig 6 (a).

Parameter	14/09	15/09	16/09	18/09	19/09	20/09	21/09
Extinction coefficient (Mm ⁻¹)	231±151	175±126	221±134	220±137	155±127	199±122	208±114
Backscatter coefficient (Mm ⁻¹ sr ⁻¹)	4.03±2.50	3.62±2.33	5.01±2.63	4.63±2.97	3.86±2.87	3.59±1.97	3.87±1.86
Lidar ratio (sr)	62±32	53±28	46±24	52±25	44±24	61±31	58±29
AOD	0.84±0.65	0.74±0.32	0.86±0.41	1.00±0.61	0.64±0.44	0.72±0.33	0.95±0.31
Height (km)	6.14±3.13	5.63±2.7	5.29±2.39	5.23±2.78	5.25±2.22	7.19±3.12	6.89±3.31
Relative humidity (%)	43±22	40±26	38±24	39±21	43±15	60±16	61±13

380 As the extensive properties of lidar measurements, the extinction coefficient and the backscatter coefficient can represent smoke concentrations. Comprehensively considering the variations in the means and the medians of these two properties during the transport, it can be found that the extensive properties of the smoke layers on 16 and 18 September were obviously higher than those of the preceding and the subsequent cross-sections, indicating higher smoke concentrations. This can also be observed in the cross-sections of 16 and 18 September in Fig. 6 (a), which include more bins with high extinction values ranging from 300 Mm⁻¹ to 400 Mm⁻¹ (indicated by yellow). The high smoke concentrations could result from the potential accumulation of smoke aerosols when they were transported to above the Atlantic. This phenomenon agrees well with the findings from the analysis of the MODIS AOD and MERRA-2 smoke CMC across the entire transport region, as illustrated in Fig. 2 (a) and (b) and the accompanying descriptions. As for the variations in the lidar ratio, one of the intensive properties that is independent of aerosol concentrations, it presents the properties of smoke aerosols in different transport phases. The average lidar ratios present a general decline tendency from 62 sr on 14 September to 44 sr on 19 September, as the transport from the west US to the mid-Atlantic occurred. Subsequently, after being transported to Europe and thereby elevated over cloud layers, the lidar ratios turned to increase to around 60 sr on 20 and 21 September, which might be explained by the changing relative humidity during and after the process of rising. The smoke layer heights infer the evidence that the layers were primarily in the troposphere during the transport. Regarding the mean values, the decline from 6.14 km on 14 to 5.25 km on 19 September may illustrate that the layers settled slightly during the transport of the high-concentration smoke aerosol. However, 7.19 km on 20 September and 6.89 on 21 September suggest that these layers were lifted after being transported to above the Europe. We also provide the relative humidity statistics of the smoke layers to provide ambient information. The smoke layers appear to gradually become drier, with an average relative humidity of 43 % on 14 varying to 39 % on 18. After being separated as the northern portion and lifted above the clouds, the relative humidity of the smoke layers turned out to increase to around 60% on 20 and 21 September, which could be the reason for the altered lidar ratio.

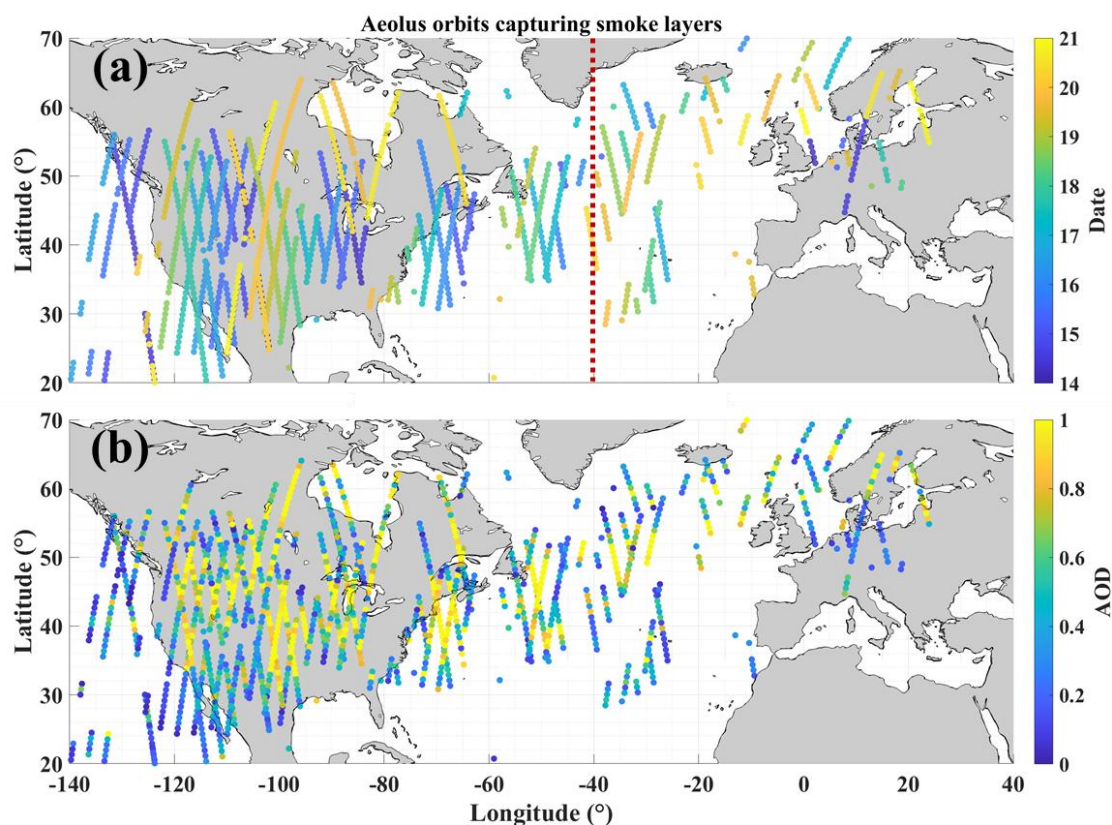
In this section, seven descending Aeolus measurements were selected to characterize the cross-sections of the smoke plume during transport. These measurements are considered representative for different transport phases of the same plume, as



confirmed by HYSPLIT trajectory simulations. However, they only provide a limited depiction of the entire smoke plume, which can extend over several thousand kilometers.

405 5.2 Features of the entire smoke event

In this section, all smoke layers identified in the ALAIN measurement cross-sections from 14 to 21 September 2020, within the region from 140°W to 40°E and 20°N to 70°N, are presented together with their statistical results. These analyses aim to investigate the evolution of the entire smoke event throughout its transport pathway.

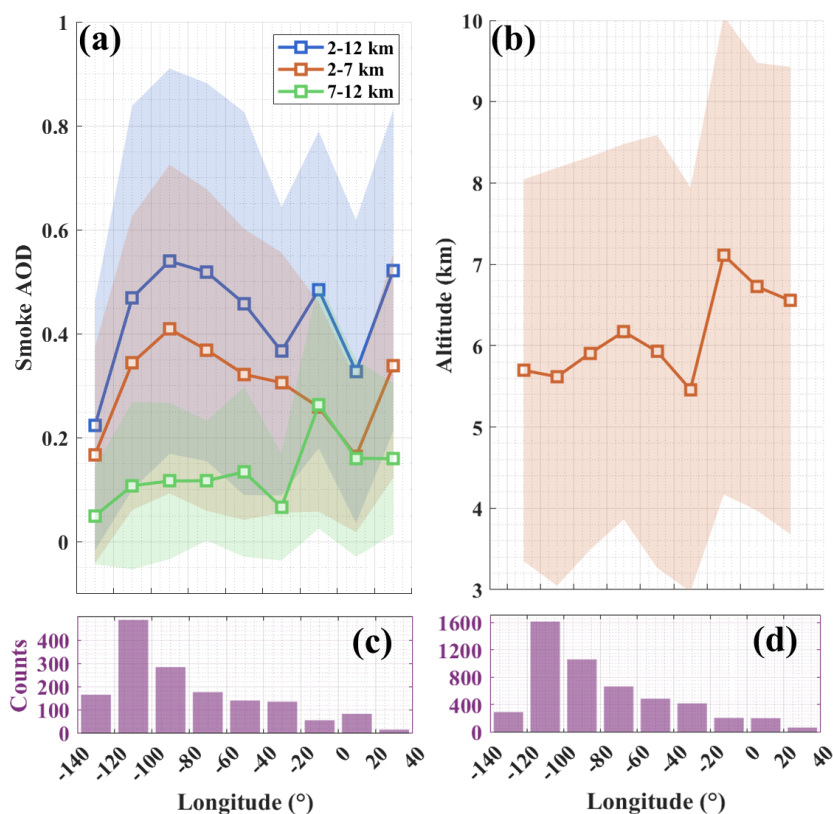


410 **Figure 8. Smoke layers captured by ALADIN along the Aeolus orbits, with the color of the tracks representing (a) observational time and (b) AOD.**

Figure 8 shows the smoke layers captured by ALADIN. The colors in the panel (a) indicate the observational time from 14 to 21 September 2020, while the colors in the panel (b) show the smoke AOD. Firstly, it can be found that the panel (a) is separated by a red dotted line. In the left side of the dotted line, it can be seen that blue and green tracks dominate the region of 140°W to 40°W. This illustrates that the smoke plumes were observed in this region from 14 to 18 September, suggesting that the smoke plumes were transported there during this period. There are also several yellow tracks in the continental US region, indicating that smoke aerosols were still being generated by wildfires from 19 to 21 September. However, they were spread above the land but they might not have been transported to the Atlantic. To the right of the red dotted line, more yellow



orbits appear from the mid-Atlantic region to northern Europe, implying the smoke plume moved along this pathway from 19
420 to 21 September. It can be also clearly found that the smoke plume separated above the mid-Atlantic around 18 to 19 September.
The movement of the smoke plume observed by Aeolus aligns well with the smoke CMC maps shown in Fig. 5. Although
daily MODIS AOD can provide photo-like observations of smoke plumes over large horizontal regions, they are quite cloud-
sensitive that the smoke plume above the northern Europe on 20 and 21 September cannot be recorded due to the cloud cover
(shown in Fig. A1). We believe that Aeolus lidar observations are capable to identify a smoke layer even if thin clouds are
425 present in a given profile. As shown in panel (b) of Fig. 8, several high AOD values were observed above Northern Europe.
In general, the bright yellow colors in the panel (b) indicate the main pathway of the smoke plume. The separated southern
smoke plume, with the major AOD below 0.6, is inferred to be weaker than the northern one. The Aeolus smoke dataset does
not present the transport of the southern plume near the Sahara Desert because it is mixed with dust aerosols, which results in
its exclusion from the dataset, as described in Section 4.2.



430

Figure 9. Statistical results (means and standard deviations) of (a) smoke AOD, (b) lidar ratio and altitude along longitude. (c)(d) The corresponding data counts of the statistics. The statistics were calculated by using the Aeolus smoke dataset (within the altitude range of 2 km to 12 km) in the period of 14 to 21 September 2020, in the smoke plume transport region of 140°W to 40°E and 20°N to 70N, and with the longitude grid of 20°.



435 To further quantitatively characterize the features of the smoke event during transport, the statistics of the AOD, layer altitude, extinction coefficient and lidar ratio were calculated along the longitude and altitude, shown in Fig. 9 through Fig. 11, respectively. Aeolus smoke data bins within the altitude range of 2 km to 12 km were selected for the analysis. The chosen altitude range was selected because (1) this smoke transport event occurred mainly below 12 km (see Fig. 7e), which approximately corresponds to the typical tropopause height in mid-latitudes, and (2) it minimizes the influence of other aerosol
440 types present in the planetary boundary layer (e.g., continental pollution and marine aerosols). In addition, for all parameters except AOD, only the data bins with extinction greater than 30 Mm^{-1} and backscatter greater than $1 \text{ Mm}^{-1}\text{sr}^{-1}$ were considered representative of smoke layers and used in the statistical calculation. Since the entire smoke plume moved eastward, the statistical values along the longitude are likely to reflect the characteristics of the smoke event along its transport pathway.

In Fig. 9, using the Aeolus smoke dataset in the period of 14 to 21 September 2020, in the smoke plume transport region of
445 140°W to 40°E and 20°N to 70°N , the means and the standard deviations of AOD (panel (a)) and altitude (panel (b)) were calculated with the longitude grid of 20° . The corresponding data counts are shown in panels (c) and (d). In panel (a), we present the variations of total AOD (2 km to 12 km), AOD within 2 to 7 km (AOD_M , corresponding to the mid-troposphere) and AOD within 7 to 12 km (AOD_U , corresponding to the upper-troposphere), indicated by the blue, red and green curves individually. In general, the total AOD exhibits a decline tendency, dropping from around 0.54 to below 0.33 in the main
450 transport region between 100°W and 20°E . The AOD_M shows a similar trend, suggesting that the smoke layers in the mid-troposphere weaken during transport. However, for the AOD_U , the slight increasing trend within 120°W to 40°W indicates that a few smoke aerosols were injected into the upper-troposphere from the mid-troposphere while the smoke plume was being transport in this region. The relatively large decline in AOD_U , from around 0.13 to below 0.07, occurred after plume separation in the region of 40°W to 20°W . After being transported above Europe, the AOD_U increased rapidly to around 0.26
455 in the region of 20°W to 0° . Regarding to the average altitudes, basically, they show an ascending trend from around 5.6 km to around 6 km in the region of 140°W to 40° , which corresponds to the increasing AOD_U in this region. A descent to below 5.5 km appeared in the plume separation region between 40°W and 20°W . Subsequently, the average altitudes turned to increase to over 7.1 km upon reaching Europe. Comprehensively considering the variations in the average AOD and altitude along the smoke transport pathway, it can be inferred that, in general, the smoke plume within 2 km to 12 km (typical altitude
460 range of free troposphere) was weakened but lifted. Nevertheless, distinct abnormal tendencies of AOD_U and layer altitude occurred in the region of 40°W to 20°W , which may be related to the mechanism of the plume separation.

Figure 10 shows the variation in smoke lidar ratio along longitude. Basically, the mean lidar ratio range of 44 sr to 51 sr is reasonable for smoke aerosol (Floutsi et al., 2023). Initially, the mean values decrease from over 50 sr in the continental US (120°W to 80°W) to around 45 sr over the mid-Atlantic (60°W to 20°W). Subsequently, they turned to rise to nearly 50 sr after
465 reaching Europe. It should be noted that the lowest mean lidar ratio, 44.6 sr, appeared in the region of 40°W to 20°W , which may also be related to the plume separation. The impact of the backscatter correction based on an assumed constant depolarization ratio on the smoke lidar ratio has been discussed in Section 4.2. A mean depolarization ratio variation of around 0.01 could induce a lidar ratio variation of around 1 sr, which has a negligible impact on the total lidar ratio variation. Thus, it



is considered that the mean lidar ratio shown in Fig. 10 is capable to be representative of the property variation of the smoke
470 event along the transport pathway.

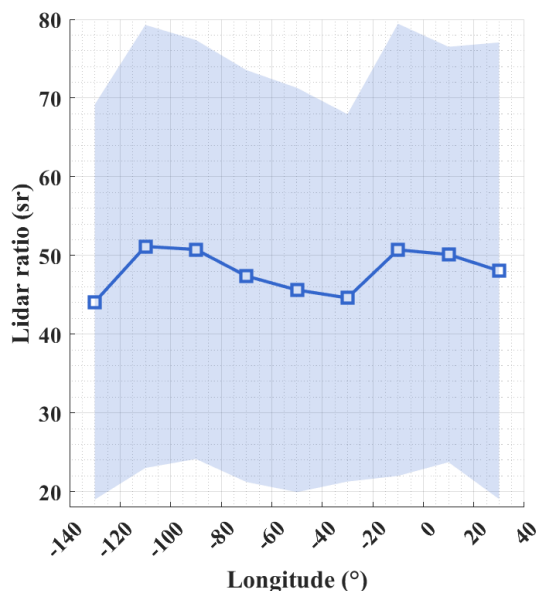


Figure 10. Statistical results (means and standard deviations) of smoke lidar ratio along longitude. The statistics were calculated by using the Aeolus smoke dataset (within the altitude range of 2 km to 12 km) in the period of 14 to 21 September 2020, in the smoke plume transport region of 140°W to 40°E and 20°N to 70N, and with the longitude grid of 20°.

475 6 Summary

Spaceborne lidar observations are well suited for studying the large-scale aerosol transport, because they have the potential to acquire cross-sections of aerosol plume during different transport phases. Although the Atmospheric Laser Doppler Instrument (ALADIN) onboard the Aeolus satellite was designed as a wind measurement lidar, it has been capable of providing aerosol profiles as a high spectral resolution lidar. These profiles can be used to investigate aerosol transport.

480 In this study, targeting the wildfire season of the West Coast of the US in September 2020, a comprehensive investigation on an intense transatlantic smoke transport was conducted, based on the Aeolus observation, synergic with another spaceborne lidar CALIOP (Cloud-Aerosol Lidar with Orthogonal Polarization), spaceborne passive instruments (Visible Infrared Imaging Radiometer Suite, VIIRS; Moderate-resolution Imaging Spectroradiometer, MODIS) and models (Modern-Era Retrospective analysis for Research and Applications, Version 2, MERRA-2; Hybrid Single Particle Lagrangian Integrated Trajectory Model,
485 HYSPLIT). The smoke plume transport event was determined starting from the west coast of the US on around 14 September, crossing the Atlantic, finally arriving above the Europe on 21 September. In order to derive a smoke dataset of extinction coefficient, backscatter coefficient and lidar ratio from Aeolus, a collocation dataset comprising Aeolus observations, MODIS AOD, and MERRA-2 smoke column mass concentration (CMC) was established. Subsequently, the method for the derivation



of smoke data from ALADIN observations was highlighted, including 1) bins selection, 2) cloud screening, 3) smoke profile
490 selection, 4) backscatter correction and 5) lidar ratio calculation. The reliability of the Aeolus smoke dataset was validated by
the comparison of AOD with MODIS measurement.

In terms of the characterization of the smoke transport, seven cross-sections on 14, 15, 16, 18, 19, 20 and 21 September, located
from the west of the US eastwards to the Europe, were preliminarily selected. HYSPLIT trajectory simulations have been used
to confirm the representativeness of these cross-sections for the smoke transport event. The specific transport pathway was
495 described in detail by these cross-sections with vertical structure. This massive smoke event was found mainly transported in
the free troposphere. The potential smoke aerosol accumulation during transport was observed in the cross-sections on 16 and
18 September, corresponding well to the AOD and CMC maps. That smoke layers ascended above cloud layers over Europe
was implied by the cross-sections on 20 and 21 September. Statistics of each cross-sections were also presented and analyzed.
Moreover, the features of the entire smoke plume during transport were investigated using the Aeolus smoke dataset from 14
500 to 21 September 2020, in the transport region. This dataset included all smoke layers captured by Aeolus along its orbits. We
highlight the ability of Aeolus to measurement aerosol layers even if in the presence of thin clouds, providing more information
than passive instruments like MODIS, which are sensitive to cloud contamination. Based on the Aeolus smoke dataset, we
further characterized the smoke plumes along the transport pathway using statistics of AOD, altitude, and lidar ratio. In general,
the AOD decreased along the pathway as the smoke plume dispersed during transport. In addition, the growing AOD in the
505 upper-troposphere (AOD_U , at altitudes ranging from 7 km to 12 km) and the ascending layer altitudes along the longitude both
indicates the smoke plume was gradually lifted during transport. The mean lidar ratios were within a reasonable range of 44
sr to 51 sr for smoke aerosol, showing a general decreasing-increasing trend along the transport pathway. Notably, the lowest
values of AOD_U , layer altitude and lidar ratio along the main pathway (120°W to 40°W) appeared within the region of 40°W
to 20°W . This may be related to the plume separation that occurred in this region.

510 In conclusion, we demonstrated that Aeolus can provide reliable observation of smoke transport event with the synergy of
multi-platform data. We believe that the comprehensive characterization of this large-scale transatlantic smoke transport event
by a spaceborne high spectral resolution lidar (HSRL) provides valuable information for global aerosol research, particularly
highlighting the capabilities of lidars to provide vertically resolved information. In the future, the synergy of multi-spaceborne
HSRL missions (the Aerosol and Carbon Detection Lidar (ACDL) at 532 nm, the ATmospheric LIDar (ATLID) at 355 nm,
515 and the wind and aerosol lidar onboard the future Aeolus follow-on mission) has great potential for the large-scale aerosol
transport research with multi-wavelength observations and dynamic field measurements.



Appendix

Longitude ranges of Sub-regions	140°W -	120°W -	100°W -80°W	80°W- 60°W	60°W- 40°W	40°W- 20°W	20°W- 0°	0°- 20°W	20°- 40°W
Depolarization ratio (mean ± std)	0.119± 0.087	0.117± 0.088	0.119± 0.088	0.114± 0.088	0.116± 0.087	0.111± 0.083	0.110± 0.083	0.110± 0.085	0.116± 0.086

Table A1. Depolarization ratio at 532 nm of the smoke plume during transport from 140° to 40°E, derived from CALIOP observations.

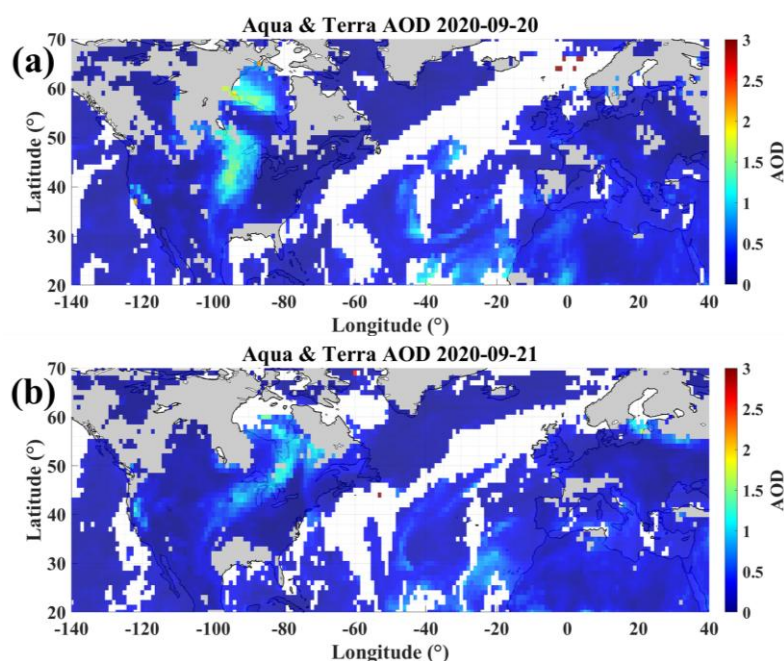


Figure A1. Average AOD from both Aqua and Terra on (a) 20 and (b) 21 September 2020.

Data availability

The Aeolus data were downloaded via the website <https://aeolus-ds.eo.esa.int/oads/access> (last access: 1 February 2026). The CALIOP data were downloaded from <https://www.earthdata.nasa.gov> (last access: 1 February 2026). The VIIRS products were acquired from <https://worldview.earthdata.nasa.gov> (last access: 1 February 2025). Data from MODIS and MERRA-2 were downloaded via <https://giovanni.gsfc.nasa.gov/giovanni> (last access: 1 February 2026). The HYSPLIT models were conducted in the website <https://www.ready.noaa.gov/hypub-bin/trajtype.pl?runtype=archive> (last access: 1 February 2026).



Author contribution

SW, KS and GD conceived the study; KS conducted the experiments and wrote the manuscript; DT and HB contributed to the
530 data analysis; all co-authors discussed the results and revised the manuscript.

Competing interests

The authors declare that they have no conflict of interest.

Funding

This research was jointly funded by the National Key Research and Development Program of China, grant number
535 2024YFF0726403, the National Natural Science Foundation of China, grant number 42475145 and U2106210, and the Hainan
Province Science and Technology Special Fund, grant number ZDYF2024GXJS012.

Acknowledgements

This study was supported by the Dragon 6 program, which is conducted by the European Space Agency and the China Science
and Technology Exchange Center (grant no. 95376). Kangwen Sun appreciates the support from the China Scholarship Council
540 (CSC) to conduct this research under the CSC no. 202306330054.

References

- Ansmann, A., Wandinger, U., Le Rille, O., Lajas, D., and Straume, A. G.: Particle backscatter and extinction profiling with
the spaceborne high-spectral-resolution Doppler lidar ALADIN: methodology and simulations, *Appl. Optics*, 46, 6606,
<https://doi.org/10.1364/AO.46.006606>, 2007.
- 545 Ansmann, A., Jimenez, C., Roschke, J., Bühl, J., Ohneiser, K., Engelmann, R., Radenz, M., Griesche, H., Hofer, J., Althausen,
D., Knopf, D. A., Dahlke, S., Gaudek, T., Seifert, P., and Wandinger, U.: Impact of wildfire smoke on Arctic cirrus formation
– Part 1: Analysis of MOSAiC 2019–2020 observations, *Atmos. Chem. Phys.*, 25, 4847–4866, <https://doi.org/10.5194/acp-25-4847-2025>, 2025.
- Ångström, A. (1964), The parameters of atmospheric turbidity. *Tellus*, 16: 64-75. <https://doi.org/10.1111/j.2153-3490.1964.tb00144.x>
550
- Baars, H., Ansmann, A., Ohneiser, K., Haarig, M., Engelmann, R., Althausen, D., Hanssen, I., Gausa, M., Pietruczuk, A.,
Szkop, A., Stachlewska, I. S., Wang, D., Reichardt, J., Skupin, A., Mattis, I., Trickl, T., Vogelmann, H., Navas-Guzmán, F.,
Haefele, A., Acheson, K., Ruth, A. A., Tatarov, B., Müller, D., Hu, Q., Podvin, T., Goloub, P., Veselovskii, I., Pietras, C.,



- Haeffelin, M., Fréville, P., Sicard, M., Comerón, A., Fernández García, A. J., Molero Menéndez, F., Córdoba-Jabonero, C.,
555 Guerrero-Rascado, J. L., Alados-Arboledas, L., Bortoli, D., Costa, M. J., Dionisi, D., Liberti, G. L., Wang, X., Sannino, A.,
Papagiannopoulos, N., Boselli, A., Mona, L., D'Amico, G., Romano, S., Perrone, M. R., Belegante, L., Nicolae, D., Grigorov,
I., Gialitaki, A., Amiridis, V., Soupiona, O., Papayannis, A., Mamouri, R.-E., Nisantzi, A., Heese, B., Hofer, J., Schechner, Y.
Y., Wandinger, U., and Pappalardo, G.: The unprecedented 2017–2018 stratospheric smoke event: decay phase and aerosol
properties observed with the EARLINET, *Atmos. Chem. Phys.*, 19, 15183–15198, <https://doi.org/10.5194/acp-19-15183-2019>,
560 2019.
- Baars, H., Radenz, M., Floutsi, A. A., Engelmann, R., Althausen, D., Heese, B., et al. (2021). Californian wildfire smoke over
Europe: A first example of the aerosol observing capabilities of Aeolus compared to ground-based lidar. *Geophysical Research
Letters*, 48, e2020GL092194. <https://doi.org/10.1029/2020GL092194>.
- Beer, C. G., Hendricks, J., and Righi, M.: A global climatology of ice-nucleating particles under cirrus conditions derived from
565 model simulations with MADE3 in EMAC, *Atmos. Chem. Phys.*, 22, 15887–15907, <https://doi.org/10.5194/acp-22-15887-2022>, 2022.
- Beer, C. G., Hendricks, J., and Righi, M.: Impacts of ice-nucleating particles on cirrus clouds and radiation derived from global
model simulations with MADE3 in EMAC, *Atmos. Chem. Phys.*, 24, 3217–3240, <https://doi.org/10.5194/acp-24-3217-2024>,
2024.
- 570 Ceamanos, X., Coopman, Q., George, M. et al. Remote sensing and model analysis of biomass burning smoke transported
across the Atlantic during the 2020 Western US wildfire season. *Sci Rep* 13, 16014 (2023). <https://doi.org/10.1038/s41598-023-39312-1>.
- Chipade, R.A.; Pandya, M.R. Theoretical derivation of aerosol lidar ratio using Mie theory for CALIOP-CALIPSO and OPAC
aerosol models. *Atmos. Meas. Tech.* 2023, 16, 5443–5459.
- 575 Cunningham, C., Williamson, G., and Bowman, D.: Increasing frequency and intensity of the most extreme wildfires on Earth,
Nat. Ecol. Evol., 12, 1420–1425, <https://doi.org/10.1038/s41598-024-02452-2>, 2024.
- Dabas, A., Denneulin, M. L., Flamant, P., Loth, C., Garnier, A., and Dolfi-Bouteyre, A.: Correcting winds measured with a
Rayleigh Doppler lidar from pressure and temperature effects, *Tellus A*, 60, 206–215, <https://doi.org/10.1111/j.1600-0870.2007.00284.x>, 2008.
- 580 Ditas, J., Ma, N., Zhang, Y., Assmann, D., Neumaier, M., Riede, H., Karu, E., Williams, J., Scharffe, D., Wang, Q., Saturno,
J., Schwarz, J. P., Katich, J. M., McMeeking, G. R., Zahn, A., Hermann, M., Brenninkmeijer, C. A. M., Andreae, M. O., Pöschl,
U., Su, H., and Cheng, Y.: Strong impact of wildfires on the abundance and aging of black carbon in the lowermost stratosphere,
P. Natl. Acad. Sci. USA, 115, E11595–E11603, <https://doi.org/10.1073/pnas.1806868115>, 2018.
- Eck, T. F., Holben, B. N., Reid, J. S., Sinyuk, A., Giles, D. M., Arola, A., Slutsker, I., Schafer, J. S., Sorokin, M. G., Smirnov,
585 A., LaRosa, A. D., Kraft, J., Reid, E. A., O'Neill, N. T., Welton, E. J., and Menendez, A. R.: The extreme forest fires in
California/Oregon in 2020: Aerosol optical and physical properties and comparisons of aged versus fresh smoke, *Atmos.
Environ.*, 305, 119798, <https://doi.org/10.1016/j.atmosenv.2023.119798>, 2023.



- Eggers, N., Graßl, S., & Ritter, C. (2024). Assessment of Hygroscopic Behavior of Arctic Aerosol by Contemporary Lidar and Radiosonde Observations. *Remote Sensing*, 16(16), 3087. <https://doi.org/10.3390/rs16163087>
- 590 Ehlers, F., Flament, T., Dabas, A., Trapon, D., Lacour, A., Baars, H., and Straume-Lindner, A. G.: Optimization of Aeolus' aerosol optical properties by maximum-likelihood estimation, *Atmos. Meas. Tech.*, 15, 185–203, <https://doi.org/10.5194/amt-15-185-2022>, 2022.
- Eitan Hirsch, Ilan Koren, Record-breaking aerosol levels explained by smoke injection into the stratosphere. *Science* 371, 1269-1274(2021). DOI:10.1126/science.abe1415.
- 595 Flamant, P. H., Cuesta, J., Denneulin, M.-L., Dabas, A., and Huber, D.: ADM-Aeolus retrieval algorithms for aerosol and cloud products, *Tellus A*, 60, 273–286, <https://doi.org/10.1111/j.1600-0870.2007.00287.x>, 2008.
- Flament, T., Trapon, D., Lacour, A., Dabas, A., Ehlers, F., and Huber, D.: Aeolus L2A aerosol optical properties product: standard correct algorithm and Mie correct algorithm, *Atmos. Meas. Tech.*, 14, 7851–7871, <https://doi.org/10.5194/amt-14-7851-2021>, 2021.
- 600 Floutsis, A. A., Baars, H., Engelmann, R., Althausen, D., Ansmann, A., Bohlmann, S., Heese, B., Hofer, J., Kanitz, T., Haarig, M., Ohneiser, K., Radenz, M., Seifert, P., Skupin, A., Yin, Z., Abdullaev, S. F., Komppula, M., Filioglou, M., Giannakaki, E., Stachlewska, I. S., Janicka, L., Bortoli, D., Marinou, E., Amiridis, V., Gialitaki, A., Mamouri, R.-E., Barja, B., and Wandinger, U.: DeLiAn – a growing collection of depolarization ratio, lidar ratio and Ångström exponent for different aerosol types and mixtures from ground-based lidar observations, *Atmos. Meas. Tech.*, 16, 2353–2379, [https://doi.org/10.5194/amt-16-2353-](https://doi.org/10.5194/amt-16-2353-2023)
- 605 2023, 2023.
- Foken, T. *Springer Handbook of Atmospheric Measurements*, 1st ed.; Springer: Cham, Switzerland, 2021. <https://doi.org/10.1007/978-3-030-52171-4>.
- Forbes, R. M. Ahlgrimm, O. Stiller, S. Di Michele and J. Delanoe, 2009: Validation of cloud parametrization. WP-2100 report for the ESA project QuARL - 21613/08/NL/CB (available from ECMWF, Reading, UK), 49 pp.
- 610 <https://www.ecmwf.int/sites/default/files/elibrary/2009/9438-validation-cloud-parametrization.pdf>, last access: 4 September 2025
- Gelaro, R., and Coauthors, 2017: The Modern-Era Retrospective Analysis for Research and Applications, Version 2 (MERRA-2). *J. Climate*, 30, 5419–5454, <https://doi.org/10.1175/JCLI-D-16-0758.1>.
- Gkikas, A., Gialitaki, A., Binietoglou, I., Marinou, E., Tsiachla, M., Siomos, N., Paschou, P., Kampouri, A., Voudouri, K. A., Proestakis, E., Mylonaki, M., Papanikolaou, C.-A., Michailidis, K., Baars, H., Straume, A. G., Balis, D., Papayannis, A., Parrinello, T., and Amiridis, V.: First assessment of Aeolus Standard Correct Algorithm particle backscatter coefficient retrievals in the eastern Mediterranean, *Atmos. Meas. Tech.*, 16, 1017–1042, <https://doi.org/10.5194/amt-16-1017-2023>, 2023.
- Gumber, A., Reid, J. S., Holz, R. E., Eck, T. F., Hsu, N. C., Levy, R. C., Zhang, J., and Veglio, P.: Assessment of severe aerosol events from NASA MODIS and VIIRS aerosol products for data assimilation and climate continuity, *Atmos. Meas. Tech.*, 16, 2547–2573, <https://doi.org/10.5194/amt-16-2547-2023>, 2023.
- 620



- Haarig, M., Ansmann, A., Baars, H., Jimenez, C., Veselovskii, I., Engelmann, R., and Althausen, D.: Depolarization and lidar ratios at 355, 532, and 1064 nm and microphysical properties of aged tropospheric and stratospheric Canadian wildfire smoke, *Atmos. Chem. Phys.*, 18, 11847–11861, <https://doi.org/10.5194/acp-18-11847-2018>, 2018.
- Hu, Q., Goloub, P., Veselovskii, I., and Podvin, T.: The characterization of long-range transported North American biomass burning plumes: what can a multi-wavelength Mie–Raman-polarization-fluorescence lidar provide?, *Atmos. Chem. Phys.*, 22, 5399–5414, <https://doi.org/10.5194/acp-22-5399-2022>, 2022.
- Hunt, W. H., D. M. Winker, M. A. Vaughan, K. A. Powell, P. L. Lucker, and C. Weimer, 2009: CALIPSO Lidar Description and Performance Assessment. *J. Atmos. Oceanic Technol.*, 26, 1214–1228, <https://doi.org/10.1175/2009JTECHA1223.1>.
- Kim, M.-H., Omar, A. H., Tackett, J. L., Vaughan, M. A., Winker, D. M., Trepte, C. R., Hu, Y., Liu, Z., Poole, L. R., Pitts, M. C., Kar, J., and Magill, B. E.: The CALIPSO version 4 automated aerosol classification and lidar ratio selection algorithm, *Atmos. Meas. Tech.*, 11, 6107–6135, <https://doi.org/10.5194/amt-11-6107-2018>, 2018.
- Kirchmeier-Young, M. C., Gillett, N. P., Zwiers, F. W., Cannon, A. J., and Anslow, F. S.: Attribution of the influence of human-induced climate change on an extreme fire season, *Earths Future*, 7, 2–10, <https://doi.org/10.1029/2018EF001050>, 2019.
- Khaykin, S., Legras, B., Bucci, S., Sellitto, P., Isaksen, L., Tencé, L., Bekki, S., Bourassa, A., Rieger, L., Zawada, D., Jumelet, J., and Godin-Beekmann, S.: The 2019/20 Australian wildfires generated a persistent smoke-charged vortex rising up to 35km altitude, *Nature Communications Earth and Environment*, 1, 22, <https://doi.org/10.1038/s43247-020-00022-5>, 2020.
- Levy, R. C., Mattoo, S., Munchak, L. A., Remer, L. A., Sayer, A. M., Patadia, F., and Hsu, N. C.: The Collection 6 MODIS aerosol products over land and ocean, *Atmos. Meas. Tech.*, 6, 2989–3034, <https://doi.org/10.5194/amt-6-2989-2013>, 2013.
- Liu H, Remer L A, Huang J, et al. Preliminary evaluation of S-NPP VIIRS aerosol optical thickness[J]. *Journal of Geophysical Research: Atmospheres*, 2014, 119(7): 3942-3962.
- Lohmann, U. and Neubauer, D.: The importance of mixed-phase and ice clouds for climate sensitivity in the global aerosol–climate model ECHAM6-HAM2, *Atmos. Chem. Phys.*, 18, 8807–8828, <https://doi.org/10.5194/acp-18-8807-2018>, 2018.
- Lux, O., Lemmerz, C., Weiler, F., Marksteiner, U., Witschas, B., Rahm, S., Geiß, A., and Reitebuch, O.: Intercomparison of wind observations from the European Space Agency's Aeolus satellite mission and the ALADIN Airborne Demonstrator, *Atmos. Meas. Tech.*, 13, 2075–2097, <https://doi.org/10.5194/amt-13-2075-2020>, 2020.
- Mamouri, R.-E., Ansmann, A., Ohneiser, K., Knopf, D. A., Nisantzi, A., Bühl, J., Engelmann, R., Skupin, A., Seifert, P., Baars, H., Ene, D., Wandinger, U., and Hadjimitsis, D.: Wildfire smoke triggers cirrus formation: lidar observations over the eastern Mediterranean, *Atmos. Chem. Phys.*, 23, 14097–14114, <https://doi.org/10.5194/acp-23-14097-2023>, 2023.
- Ohneiser, K., Ansmann, A., Kaifler, B., Chudnovsky, A., Barja, B., Knopf, D. A., Kaifler, N., Baars, H., Seifert, P., Villanueva, D., Jimenez, C., Radenz, M., Engelmann, R., Veselovskii, I., and Zamorano, F.: Australian wildfire smoke in the stratosphere: the decay phase in 2020/2021 and impact on ozone depletion, *Atmos. Chem. Phys.*, 22, 7417–7442, <https://doi.org/10.5194/acp-22-7417-2022>, 2022.



- Ohneiser, K., Ansmann, A., Witthuhn, J., Deneke, H., Chudnovsky, A., Walter, G., and Senf, F.: Self-lofting of wildfire smoke
655 in the troposphere and stratosphere: simulations and space lidar observations, *Atmos. Chem. Phys.*, 23, 2901–2925,
<https://doi.org/10.5194/acp-23-2901-2023>, 2023.
- Omar, A. H., Winker, D. M., Kittaka, C., Vaughan, M. A., Liu, Z., Hu, Y., Trepte, C. R., Rogers, R. R., Ferrare, R. A., Lee,
K.-P., Kuehn, R. E., and Hostetler, C. A.: The CALIPSO Automated Aerosol Classification and Lidar Ratio Selection
Algorithm, *J. Atmos. Ocean. Tech.*, 26, 1994–2014, <https://doi.org/10.1175/2009JTECHA1231.1>, 2009.
- 660 Paschou, P., Siomos, N., Tsekeri, A., Louridas, A., Georgoussis, G., Freudenthaler, V., Binietoglou, I., Tsaknakis, G.,
Tavernarakis, A., Evangelatos, C., von Bismarck, J., Kanitz, T., Meleti, C., Marinou, E., and Amiridis, V.: The eVe reference
polarisation lidar system for the calibration and validation of the Aeolus L2A product, *Atmos. Meas. Tech.*, 15, 2299–2323,
<https://doi.org/10.5194/amt-15-2299-2022>, 2022.
- Peterson, D.A., Fromm, M.D., McRae, R.H.D. *et al.* Australia’s Black Summer pyrocumulonimbus super outbreak reveals
665 potential for increasingly extreme stratospheric smoke events. *npj Clim Atmos Sci* 4, 38 (2021).
<https://doi.org/10.1038/s41612-021-00192-9>.
- Reitebuch, O.: The Spaceborne Wind Lidar Mission ADM-Aeolus, in: *Atmospheric Physics, Research Topics in Aerospace*,
edited by: Schumann, U., ISBN 978-3-642-30182-7, Springer-Verlag Berlin Heidelberg, 815–827,
https://doi.org/10.1007/978-3-642-30183-4_49, 2012.
- 670 Rennie, M., Tan, D., Andersson, E., Poli, P., Dabas, A., de Kloe, J., Marseille, G., and Stoffelen, A.: Aeolus Level-2B
Algorithm Theoretical Basis Document, version 3.40, [https://earth.esa.int/documents/d/earth-
online/aeolus_l2b_algorithm_tbd-pdf](https://earth.esa.int/documents/d/earth-online/aeolus_l2b_algorithm_tbd-pdf) (last access: 28 August 2025), 2020.
- Savtchenko A, Ouzounov D, Ahmad S, et al. Terra and Aqua MODIS products available from NASA GES DAAC[J].
Advances in Space Research, 2004, 34(4): 710-714.
- 675 Shang, X., Lipponen, A., Filioglou, M., Sundström, A.-M., Parrington, M., Buchard, V., Darmenov, A. S., Welton, E. J.,
Marinou, E., Amiridis, V., Sicard, M., Rodríguez-Gómez, A., Komppula, M., and Mielonen, T.: Monitoring biomass burning
aerosol transport using CALIOP observations and reanalysis models: a Canadian wildfire event in 2019, *Atmos. Chem. Phys.*,
24, 1329–1344, <https://doi.org/10.5194/acp-24-1329-2024>, 2024.
- Sokolik, I. N., Soja, A. J., DeMott, P. J., & Winker, D. (2019). Progress and challenges in quantifying wildfire smoke emissions, their
680 properties, transport, and atmospheric impacts. *Journal of Geophysical Research: Atmospheres*, 124, 13005–
13025. <https://doi.org/10.1029/2018JD029878>.
- Stein, A.F., Draxler, R.R., Rolph, G.D., Stunder, B.J.B., Cohen, M.D., and Ngan, F., (2015). NOAA's HYSPLIT atmospheric
transport and dispersion modeling system, *Bull. Amer. Meteor. Soc.*, 96, 2059–2077, [http://dx.doi.org/10.1175/BAMS-D-14-
00110.1](http://dx.doi.org/10.1175/BAMS-D-14-00110.1).
- 685 Stoffelen, A., Pailleux, J., Källén, E., Vaughan, J. M., Isaksen, I., Flamant, P., Wergen, W., Andersson, E., Schyberg, H.,
Culoma, A., Meynart, R., Endemann, M., and Ingmann, P.: The Atmospheric Dynamics Mission For Global Wind Field
Measurement, *B. Am. Meteorol. Soc.*, 86, 73–88, <https://doi.org/10.1175/BAMS-86-1-73>, 2005.



- 690 Tan, D. G., Andersson, E., Kloe, J. D., Marseille, G.-J., Stoffelen, A., Poli, P., Denneulin, M.-L., Dabas, A., Huber, D., and
Reitebuch, O.: The ADM-Aeolus wind retrieval algorithms, *Tellus A*, 60, 191–205, <https://doi.org/10.1111/j.1600-0870.2007.00285.x>, 2008.
- Trapon, D., Baars, H., Floutsi, A. A., Bley, S., Haorig, M., Lacour, A., Flament, T., Dabas, A., Nehrir, A. R., Ehlers, F., and
Huber, D.: Cross-validations of the Aeolus aerosol products and new developments with airborne high-spectral-resolution lidar
measurements above the tropical Atlantic during JATAC, *Atmos. Meas. Tech.*, 18, 3873–3896, <https://doi.org/10.5194/amt-18-3873-2025>, 2025.
- 695 Trickl, T., Vogelmann, H., Fromm, M. D., Jäger, H., Perfahl, M., and Steinbrecht, W.: Measurement report: Violent biomass
burning and volcanic eruptions – a new period of elevated stratospheric aerosol over central Europe (2017 to 2023) in a long
series of observations, *Atmos. Chem. Phys.*, 24, 1997–2021, <https://doi.org/10.5194/acp-24-1997-2024>, 2024.
- Twohy, C. H., Toohey, D. W., Levin, E. J. T., DeMott, P. J., Rainwater, B., Garofalo, L. A., et al. (2021). Biomass burning smoke and its
influence on clouds over the western U. S. *Geophysical Research Letters*, 48,
700 e2021GL094224. <https://doi.org/10.1029/2021GL094224>
- Vaughan, G., Draude, A. P., Ricketts, H. M. A., Schultz, D. M., Adam, M., Sugier, J., and Wareing, D. P.: Transport of
Canadian forest fire smoke over the UK as observed by lidar, *Atmos. Chem. Phys.*, 18, 11375–11388,
<https://doi.org/10.5194/acp-18-11375-2018>, 2018.
- Wang, P., Donovan, D. P., van Zadelhoff, G.-J., de Kloe, J., Huber, D., and Reissig, K.: Evaluation of Aeolus feature mask
705 and particle extinction coefficient profile products using CALIPSO data, *Atmos. Meas. Tech.*, 17, 5935–5955,
<https://doi.org/10.5194/amt-17-5935-2024>, 2024.
- Winker, D. M., Vaughan, M. A., Omar, A. H., Hu, Y., Powell, K. A., Liu, Z., Hunt, W. H., and Young, S. A.: Overview of the
CALIPSO Mission and CALIOP Data Processing Algorithms, *J. Atmos. Ocean. Technol.*, 26, 2310–2323, 2009.